Nonuniform growth and surface friction determine bacterial biofilm morphology on soft substrates

Chenyi Fei[a,b], Sheng Mao[c], Jing Yan[a,c], Ricard Alert[b,d], Howard A. Stone[c], Bonnie L. Bassler[a,e], Ned S. Wingreen[a,b,d,1], and Andrej Košmrlj[c,f,1]

[a]Department of Molecular Biology, Princeton University, Princeton, NJ 08544; [b]Lewis-Sigler Institute for Integrative Genomics, Princeton University, Princeton, NJ 08544; [c]Department of Mechanical and Aerospace Engineering, Princeton University, Princeton, NJ 08544; [d]Princeton Center for Theoretical Science, Princeton University, Princeton, NJ 08544; [e]Howard Hughes Medical Institute, Chevy Chase, MD 20815; and [f]Princeton Institute for the Science and Technology of Materials, Princeton University, Princeton, NJ 08544

Edited by David A. Weitz, Harvard University, Cambridge, MA, and approved February 19, 2020 (received for review November 7, 2019)

During development, organisms acquire three-dimensional (3D) shapes with important physiological consequences. While basic mechanisms underlying morphogenesis are known in eukaryotes, it is often difficult to manipulate them in vivo. To circumvent this issue, here we present a study of developing *Vibrio cholerae* biofilms grown on agar substrates in which the spatiotemporal morphological patterns were altered by varying the agar concentration. Expanding biofilms are initially flat but later undergo a mechanical instability and become wrinkled. To gain mechanistic insights into this dynamic pattern-formation process, we developed a model that considers diffusion of nutrients and their uptake by bacteria, bacterial growth/biofilm matrix production, mechanical deformation of both the biofilm and the substrate, and the friction between them. Our model shows quantitative agreement with experimental measurements of biofilm expansion dynamics, and it accurately predicts two distinct spatiotemporal patterns observed in the experiments—the wrinkles initially appear either in the peripheral region and propagate inward (soft substrate/low friction) or in the central region and propagate outward (stiff substrate/high friction). Our results, which establish that nonuniform growth and friction are fundamental determinants of stress anisotropy and hence biofilm morphology, are broadly applicable to bacterial biofilms with similar morphologies and also provide insight into how other bacterial biofilms form distinct wrinkle patterns. We discuss the implications of forming undulated biofilm morphologies, which may enhance the availability of nutrients and signaling molecules and serve as a "bet hedging" strategy.

bacterial biofilm | wrinkling instability | chemomechanical model of growth | *Vibrio cholerae*

The intricate shapes of organisms are determined by the spatiotemporal patterns of growth as well as the mechanical properties of their underlying biological components (1–3). Three-dimensional (3D) shape transformations in developing organisms often arise via differential growth of connected tissues (1, 4). Such asymmetric growth patterns generate compressive stresses within the faster growing tissues, which may cause mechanical instabilities (5–7). Growth-induced mechanical instabilities drive the formation of many convoluted morphologies, such as the gyrification of brains (2, 8, 9), the vilification and looping of guts (10, 11), and the branching of lungs (12, 13) as well as 3D structures of synthetic systems with patterned swelling (5, 14–17).

Biofilms, which represent a predominant form of bacterial life in nature (18–20), also display a variety of 3D developmental morphologies ranging from radial stripes, to concentric rings, to disordered labyrinth and herringbone patterns (21–25). In the case of *Vibrio cholerae*, a model biofilm former, the development of wrinkled biofilm morphologies is proposed to be caused by mechanical instabilities (26). It has been demonstrated that biofilms provide a tractable experimental system for the quantitative investigation of mechanomorphogenesis (26, 27), which could shed light on complex developmental processes in higher organisms. In particular, one can readily alter bacterial biofilm morphologies by varying the agar concentration in the substrate on which biofilms are grown. Phenotypic variations in biofilm morphologies are also exploited to identify new genes and biochemical compounds that affect biofilm formation (28–30). For these reasons, it is desirable to obtain a full mechanistic understanding of biofilm morphogenesis.

The major components of the *V. cholerae* biofilm matrix and their roles in defining the biofilm's bulk and interfacial mechanical properties have been well explored (20, 31–35). *V. cholerae* biofilms behave as soft viscoelastic solids similar to hydrogels and possess finite adhesion to the agar surface on which they are grown (36). Thus, as the biofilm expands, it is mechanically constrained by the agar substrate. Mechanical compression due to constrained biofilm expansion ultimately triggers instabilities that result in out-of-plane deformation and the 3D biofilm morphology (26, 37). While a mechanical basis for instability-induced pattern formation in biofilms has been suggested previously (27, 37), the dynamics of stress accumulation during biofilm

Significance

Shape transformations during an organism's development often arise from mechanical instabilities driven by nonuniform growth. A remarkable example is the formation of 3D wrinkles in bacterial biofilms growing on soft substrates, which may enhance the availability of nutrients and signaling molecules. To investigate the formation of biofilm wrinkle patterns, we developed a chemomechanical model that incorporates nutrient-limited inhomogeneous growth, surface friction, and the ensuing mechanical stresses and deformations. We predict the spatiotemporal stress field in a growing biofilm and how it dictates the formation of 3D biofilm morphology. Our model provides insight into the observed stages of expansion of *Vibrio cholerae* biofilms and suggests that universal mechanical principles may underlie the formation of 3D morphologies in biofilms across species.

Author contributions: C.F., S.M., J.Y., H.A.S., B.L.B., N.S.W., and A.K. designed research; C.F., S.M., J.Y., R.A., N.S.W., and A.K. performed research; C.F., S.M., J.Y., R.A., H.A.S., B.L.B., N.S.W., and A.K. analyzed data; and C.F., S.M., J.Y., R.A., H.A.S., B.L.B., N.S.W., and A.K. wrote the paper.

The authors declare no competing interest.

This article is a PNAS Direct Submission.

Data deposition: All data and simulation codes used in this paper are available to the readers on GitHub: https://github.com/f-chenyi/biofilm-mechanics-theory.

[1]To whom correspondence may be addressed. Email: andrej@princeton.edu or wingreen@princeton.edu.

This article contains supporting information online at https://www.pnas.org/lookup/suppl/doi:10.1073/pnas.1919607117/-/DCSupplemental.

First published March 19, 2020.

expansion and the consequences to global pattern formation remain largely unknown.

A key to understanding the full 3D morphodynamics of *V. cholerae* biofilms involves the cells' spatially heterogeneous physiology (38). Soon after the initial expansion of the biofilm, growth occurs primarily at the edge of the biofilm due to nutrient limitation near the center (25, 26, 39–42). This finding raises the question, how does the corresponding nonuniform growth profile, combined with the mechanical interaction between the biofilm and the substrate, lead to the observed morphodynamics?

Here we present a two-dimensional (2D) chemomechanical model that quantitatively captures the multistage kinematics and morphodynamics of biofilm development. Consistent with experimentally measured velocity profiles, our model predicts three distinct kinematic stages of biofilm expansion prior to the formation of wrinkles. We also demonstrate that nonuniform growth due to nutrient depletion generates anisotropic compressive stresses in the outer biofilm region leading to radial stripes; by contrast, friction favors isotropic compressive stress in the biofilm center, leading to zigzag herringbone-like patterns. Our model reveals how mechanical stresses evolve in space and time in a growing biofilm, which explains the morphodynamics of experimental biofilms grown on substrates of different agar concentrations. Our model thus illustrates the mechanical principles underlying how growth and friction drive the emergent 3D morphologies of *V. cholerae* biofilms. These principles may be widely applicable to other bacterial biofilms, including those with distinct growth/matrix production profiles and morphologies, such as concentric rings in wild-type *Pseudomonas aeruginosa* PA14 (43) and *Escherichia coli* K-12 strain W3110 (22).

Results

Biofilm Morphodynamics Depend on Substrate Stiffness. After a liquid drop is used to inoculate *V. cholerae* on an agar substrate, a biofilm initially expands radially and remains flat with no recognizable morphological features except at the center where inoculation occurred (Fig. 1 *A* and *B*). Expansion occurs because bacteria consume nutrients from the agar substrate, proliferate, and produce extracellular matrix. Growing biofilms experience adhesion to the nongrowing agar substrate, and the sliding friction between biofilm and agar mechanically constrains biofilm expansion (*SI Appendix*, Section IIG). Thus, growing biofilms become compressed and build up mechanical stresses. When the compressive stress reaches a critical value, a mechanical instability generates wrinkles (Fig. 1*A*). Wrinkles are vertical deformations of the biofilm together with the adhered substrate with a characteristic wavelength (Fig. 1*C*) that depends on the thickness of the biofilm and on the mechanical properties of the biofilm and the agar substrate (26, 44, 45). Subsequently, as compressive stresses continue to build up, a biofilm can partially detach from the agar substrate, forming delaminated blisters (26, 27, 46). In this manuscript, we restrict our focus to exploring the original wrinkle patterns outside the inoculation core—localized cell death has been shown to facilitate pattern formation inside the inoculation core (47).

Notably, the development of wrinkle patterns depends on the stiffness of the agar substrate. For *V. cholerae*, after about 30 h of growth on soft substrates (low agar concentration), a pattern of radial wrinkles initially appears at the outer edge of the biofilm and subsequently propagates toward the center (Fig. 1 *A* and *B*, *Top*). By contrast, on stiff substrates (high agar concentration), radial wrinkles initially form near the center and propagate outward (Fig. 1 *A* and *B*, *Bottom*). A few hours later,

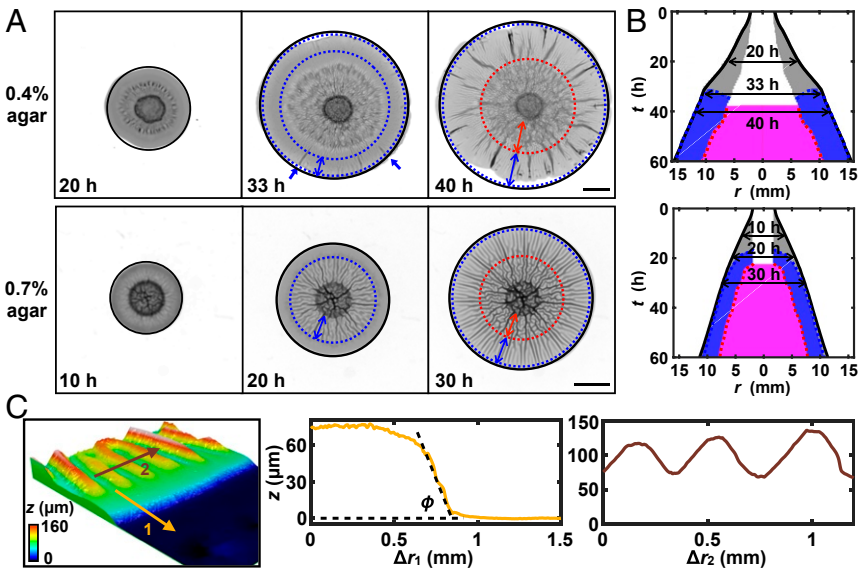

Fig. 1. Morphogenesis of *V. cholerae* biofilms grown at an air–solid interface. (*A*) Transmission images of biofilms grown on 0.4% (*Top*) and 0.7% (*Bottom*) agar substrates at the designated times, where time is measured relative to the time when a biofilm starts expanding radially. Black solid circles mark the boundaries of entire biofilms, blue dotted circles mark the boundaries of regions with radial patterns, and red dotted circles mark the boundaries of regions with zigzag patterns. Blue single-headed arrows indicate radial morphological features near the edge. Blue double-headed arrows span the regions with radial patterns. Red double-headed arrows span the regions with zigzag patterns. (Scale bars: 3 mm.) (*B*) Kymograph representation of the pattern-formation dynamics of experimental biofilms grown on 0.4% (*Top*) and 0.7% (*Bottom*) agar substrates, where r measures the distance from the center of the biofilm and t is time. Gray, blue, and magenta colors indicate regions without patterns, with radial patterns and with zigzag patterns, respectively. The internal white zone indicates the region possessing patterns related to the initial biofilm at $t = 0$. Biofilms shown in *A* are marked by horizontal double-headed arrows at the designated times. The boundaries of different regions (as outlined in *A*) were obtained based on the intensity of transmitted light (*Materials and Methods*). (*C*) (*Left*) Height map of a 3.2 mm × 2.4 mm region of the edge of a biofilm grown on 0.6% agar (t = 22 h). (*Middle* and *Right*) Height profiles corresponding to the positions spanned by the yellow (denoted by 1) and brown (denoted by 2) arrows in *Left*. Intersecting dashed lines denote the biofilm leading angle ϕ. The zero value for z was chosen to coincide with the average height of a line profile on the agar surface.

herringbone-like zigzag patterns emerge in the central region, surrounded by the outer region of radial stripes. Both of these regions expand outward at approximately the same speed as the expanding edge of the biofilm (Fig. 1*B*). In this steadily expanding state, surface profiling by confocal microscopy reveals a wedge-shaped rim (~ 200 μm in width) with a constant leading angle ϕ, followed by a narrow region (~ 500 μm in width) of nearly constant height, followed, in turn, by the region of radial stripe patterns (Fig. 1*C*).

Chemomechanical Model of Biofilm Development. To understand the observations described in the previous section, we developed a chemomechanical model of biofilm development that takes into account the diffusion of nutrients and their uptake by bacteria (Fig. 2*A*), growth of the biofilm, mechanical deformation of the biofilm and the agar substrate, and the friction between them (Fig. 2*B*). In this section, we focus on the early stage of development, when the biofilm surface is still flat. We denote by superscript 0 the deformations of the flat biofilm. The modifications of the model required to describe the wrinkled morphologies are discussed in a later section.

The kinematics of biofilm development are described by a time-varying mapping between an internal material coordinate system $\boldsymbol{X}_0$ and the laboratory frame $\boldsymbol{x}$, i.e., $\boldsymbol{x}=\boldsymbol{x}(\boldsymbol{X}_0, t)$. Following the finite-strain formalism (48), we define the deformation gradient $\mathbf{F}=\partial\boldsymbol{x}/\partial\boldsymbol{X}_0$, which captures the local change in shape and volume of a biofilm relative to its initial configuration. The overall change in shape arises from both growth and mechanical deformation. Accordingly, we follow the convention of multiplicative decomposition (49–51) and decompose $\mathbf{F}=\mathbf{F}_\mathrm{e}\cdot\mathbf{F}_\mathrm{g}$ into a contribution $\mathbf{F}_\mathrm{g}$ due to growth (which results in a postgrowth intermediate virtual configuration, where neighboring regions may overlap creating incompatibility; Fig. 2*B*) and a contribution $\mathbf{F}_\mathrm{e}$ due to elastic deformation that is required to ensure compatibility (deformed contours in Fig. 2*B*). Using this theoretical framework, we next specify our model of biofilm growth and mechanics (see also *SI Appendix*, Sections I and II, for details).

During development, *V. cholerae* biofilms on agar stabilize at a thickness of roughly 100 μm, which is set by the penetration depth of oxygen (52), and subsequently extend primarily in 2D along the substrate. In principle, rod-shaped bacteria such as *V. cholerae* can align, leading to anisotropic growth, which has important consequences for pattern formation (37, 46, 53). However, experimentation shows that bacterial cells in *V. cholerae* biofilms grown on agar do not locally order in the horizontal directions (36). Therefore, we model the growth part of the deformation gradient as $\mathbf{F}_\mathrm{g}=\begin{pmatrix}\lambda_\mathrm{g}\mathbf{I}_\parallel & \mathbf{0}\\ \mathbf{0} & 1\end{pmatrix}$, reflecting an isotropic increase in size (denoted by the 2D identity matrix $\mathbf{I}_\parallel$) in the planar direction by a factor λ_g and neglecting growth in the vertical direction (the thickness H of the undeformed biofilm is assumed to be constant). The thin-film geometry also permits a simplified 2D representation of a biofilm in which physical quantities are expressed as functions of an in-plane coordinate $\boldsymbol{x}_\parallel$.

In order to account for the inhomogeneous growth profile of experimental biofilms (26), we consider nutrient limitation of biofilm growth. Specifically, we assume that the growth rate

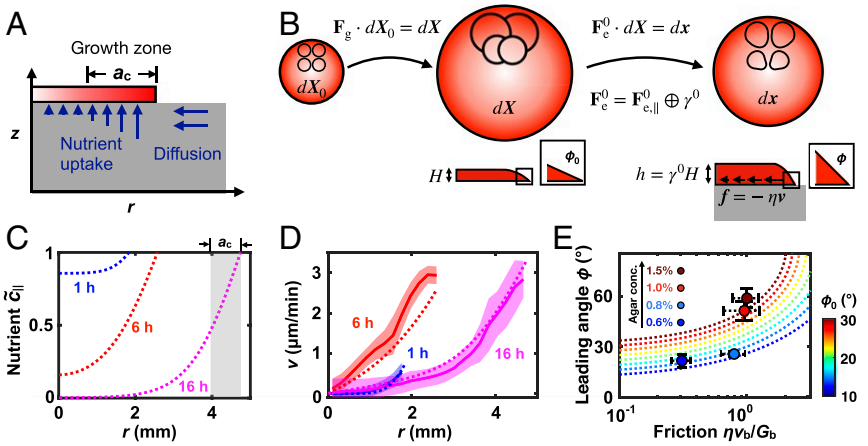

Fig. 2. A chemomechanical growth model captures the kinematics of biofilm expansion. (*A*) Schematic of nutrient diffusion-uptake dynamics. Nutrients diffuse through the agar substrate (gray) and are taken up by the bacterial biofilm (red), where blue arrows indicate the magnitudes of nutrient fluxes. Bacterial growth rate is proportional to nutrient uptake, which in turn depends on the local nutrient concentration. The established nutrient concentration profile (see *C*) sets a nutrient-rich annular periphery (its width denoted by a_c) where cells actively grow. Lighter (darker) red color indicates slower (faster) growth. r indicates the lateral distance from the center of the biofilm. (*B*) Schematic of the plane-stress elastogrowth model (color code as in *A*). Starting from an initial stress-free configuration (*Left*), local growth of the biofilm $\mathbf{F}_\mathrm{g}$ creates a virtual stress-free intermediate state (*Middle*), which is further deformed by elastic deformation $\mathbf{F}_\mathrm{e}^0$, to ensure its compatibility (no overlap between marked regions), into a stressed current configuration (*Right*). The elastic deformation $\mathbf{F}_\mathrm{e}^0$ is decomposed into an in-plane compression, denoted by $\mathbf{F}_{\mathrm{e},\parallel}^0$, and a stretch γ^0 of the film thickness H (*Bottom Right*). As the biofilm expands and moves relative to the substrate, it experiences a surface friction (black arrows) $\boldsymbol{f}=-\eta\boldsymbol{v}$, where η is the friction coefficient and $\boldsymbol{v}$ is the expansion velocity. In the bulk, friction impedes biofilm expansion and is balanced by internal stresses; at the rim, friction increases the biofilm leading angle from ϕ_0 to ϕ (*Bottom Middle* and *Bottom Right*). (*C*) Nutrient concentration $\tilde{c}_\parallel$ and (*D*) radial expansion velocity v versus the radial coordinate r at the designated times. $\tilde{c}_\parallel$ is normalized by the concentration at the edge of the biofilm. Shaded gray area in *C* indicates the active growth zone where $\tilde{c}_\parallel > 0.5$. Solid curves with shaded error bands in *D* represent experimental data (mean $\pm$ std) for a biofilm grown on a 0.7% agar substrate. The radial velocity was extracted by averaging over a ring of the biofilm at radius r from the center. Dotted curves represent simulation results for the parameters chosen by fitting the simulation velocity profiles to the experimental data (*Materials and Methods* and Fig. S1). (*E*) Theoretical predictions for the biofilm leading angle ϕ (Eq. **3**; dotted curves) as a function of the dimensionless friction $\eta v_b/G_b$ and initial angle ϕ_0 (color bar), where v_b is the expansion velocity at the biofilm's edge and G_b is the biofilm shear modulus. Theory curves are computed with the circumferential compression at the biofilm edge set to $F_{e,\theta\theta}=0.8$, but the results depend only minimally on this choice (Fig. S9). Colored circles show experimental data (mean $\pm$ std, n = 3) at the designated agar concentrations. ϕ is measured at $t=36$ h. Horizontal error bars are dashed because the friction coefficient η is not directly measured but rather is inferred by fitting (see *Materials and Methods* for details).

depends on a 2D nutrient field $c_\parallel(\boldsymbol{x}_\parallel, t)$, which follows the diffusion-uptake kinematics (41):

$$\frac{\partial c_\parallel}{\partial t} = D\nabla_\parallel^2 c_\parallel - Q_0 J_{\mathrm{e},\parallel}^{-1} \frac{c_\parallel}{(K + c_\parallel)}. \quad [1]$$

Here D is the diffusion constant, spatial derivatives are taken with respect to $\boldsymbol{x}_\parallel$, and the final term describes the uptake of nutrients by bacteria according to the Monod law (54), where K is the concentration of nutrients at the half-maximal uptake rate, Q_0 is the maximum uptake rate per unit area in the intermediate grown configuration, and the $J_{\mathrm{e},\parallel} = \det(\mathbf{F}_{\mathrm{e},\parallel})$ factor is included to account for the change in areal density of bacteria due to elastic deformation (see *Materials and Methods* and description below). The growth field $\lambda_{\mathrm{g}}(\boldsymbol{x}_\parallel, t)$ evolves in time according to the consumption of nutrients $\partial\lambda_{\mathrm{g}}/\partial t = k_{\mathrm{g}}(c_\parallel)\lambda_{\mathrm{g}}$, where the growth rate $k_{\mathrm{g}}(c_\parallel)$ is related to the Monod law described above (see *Materials and Methods* and *SI Appendix*, Section II, for details). This reduced 2D model provides a reasonable approximation to the full 3D diffusion dynamics of nutrients in the agar (*SI Appendix*, Section IIE and Figs. S2 and S3). Note that biofilm growth rate may depend on other factors in addition to nutrient availability, such as accumulation of waste products in the environment. Nevertheless, our 2D minimal model is sufficient to capture the spatially nonuniform growth that plays an essential role in biofilm morphodynamics.

Mechanically, we model the biofilm as a plane-stress thin film, where it is assumed that the stress components perpendicular to the biofilm surface are negligible. The plane-stress simplification allows for the elastic deformation $\mathbf{F}_{\mathrm{e}}^0 = \begin{pmatrix} \mathbf{F}_{\mathrm{e},\parallel}^0 & \mathbf{0} \\ \mathbf{0} & \gamma^0 \end{pmatrix}$ to be decomposed into the in-plane compression $\mathbf{F}_{\mathrm{e},\parallel}^0$ and the vertical stretch γ^0 (Fig. 2*B* and *SI Appendix*, Section IIB), leading to a quasi-2D description of a biofilm with varying thickness $h(\boldsymbol{x}_\parallel, t) = \gamma^0(\boldsymbol{x}_\parallel, t)H$.

In our model, mechanical stresses in the biofilm arise from elastic deformation and are specified by the constitutive relation $\boldsymbol{\sigma}_\parallel(\mathbf{F}_{\mathrm{e}})$, where $\boldsymbol{\sigma}_\parallel$ is the in-plane stress tensor. Biofilms are complex hydrogel-like materials, whose constitutive relations are well approximated by nearly incompressible neo-Hookean elasticity (*SI Appendix*, Section IIF and Fig. S4). Here we modeled the biofilm as an incompressible neo-Hookean elastic material (8, 10, 55), but our results are largely insensitive to any plausible choice of rheological model for the biofilm (*SI Appendix*, Section VII and Fig. S14).

We obtain the expansion velocity $\boldsymbol{v}(\boldsymbol{x}_\parallel, t)$ of a growing biofilm from a differential equation for local force balance,

$$\nabla_\parallel \cdot (h\boldsymbol{\sigma}_\parallel) - \eta\boldsymbol{v} = 0. \quad [2]$$

Here we assume that friction between the growing biofilm and the agar arises from binding and unbinding of biofilm matrix polymers with the adhesive biofilm proteins that have been secreted onto the agar surface (34). In particular, on time scales much longer than the characteristic unbinding time, the biofilm–substrate adhesive bonds undergo stick-and-slip processes leading to a form of viscous friction, and we approximate the friction coefficient η as proportional to the shear modulus G_{s} of the agar substrate (56–58) (*SI Appendix*, Section IIG and Fig. S5). The partial differential equations for this model were solved numerically in the Lagrangian coordinate system with the open source computing platform FEniCS (see *Materials and Methods* for details). All of the model parameters were estimated from the experiments (*SI Appendix*, Table S2 and Section IIC) except for the friction coefficient η and the nutrient uptake rate Q_0, which were obtained by fitting the velocity profiles in our model (see below) to experimental data (*Materials and Methods* and *SI Appendix*, Fig. S1). Next, we present model results for the early stages of biofilm development, prior to wrinkling.

Biofilm Expansion Has Three Kinematic Stages. In the model, nutrients are gradually depleted underneath the growing biofilm (Fig. 2*C*). Once a steadily expanding state is achieved after about 15 h, most of the growth is restricted to the narrow nutrient-rich zone $a_{\mathrm{c}} \approx 1\,\mathrm{mm}$ near the rim of the biofilm (Fig. 2*C* and *SI Appendix*, Fig. S3), which is consistent with experiment (26).

Our model predicts three stages of biofilm expansion with distinct radial velocity profiles $v(r, t)$ (Fig. 2*D* and *SI Appendix*, Fig. S6), where r is the distance from the center of the biofilm. In the initial stage, the interior of the biofilm is stationary while the biofilm edge moves slowly outward. The magnitude of radial velocity and the size of the moving region gradually increase until, at the second stage, the entire biofilm undergoes uniform expansion with a radial velocity v that is linearly proportional to r. At later times, in the third stage, the biofilm expansion in the central region slows due to the depletion of nutrients while the edge of the biofilm continues to move outward with a steady velocity (*SI Appendix*, Fig. S6). These three kinematic stages are also observed in experiments, and our model predictions closely match the measured velocity profiles (Fig. 2*D*).

The three kinematic stages can be understood in the following way: During the first stage, which corresponds to early times ($t \ll 1/k_{\mathrm{g}}^{\max}$ where $k_{\mathrm{g}}^{\max}$ is the maximal growth rate of a biofilm), friction with the agar substrate prevents the growing biofilm from expanding radially in the central region. As stresses gradually build up (Fig. 3 *A* and *B*), the width of the mobile annular zone at the biofilm edge increases in proportion to $(t/\eta)^{1/2}$ (*SI Appendix*, Section III and Fig. S7). The second stage ensues once this mobile zone spreads through the entire biofilm, so that the radial velocity becomes approximately a linear function of the distance from the center (Fig. 2*D* and *SI Appendix*, Section III and Fig. S8). The third stage follows once the nutrients in the central region are depleted, which slows down biofilm growth and reduces the radial velocity in that region (Fig. 2 *C* and *D*).

Higher Friction Increases the Biofilm Leading Angle. We next investigate how friction shapes the edge of an expanding biofilm. Specifically, we consider the local deformation of the wedge-shaped edge of a biofilm when sliding on a surface with velocity v_{b}. The surface provides a frictional shear force of magnitude ηv_{b} acting on the bottom of the biofilm edge and thus generates a simple shear parallel to the horizontal plane. This shear deformation increases the leading angle from ϕ_0 in the rest state to ϕ in the deformed state (Fig. 2*B*).

To quantify how the biofilm leading angle increases with friction, we decomposed the elastic part of the deformation gradient $\mathbf{F}_{\mathrm{e}}$ into the product of rotations $\mathbf{R}$ and principal stretches $\mathbf{U}$ to connect the geometry, characterized by the angles ϕ and ϕ_0, to the stress state of the biofilm edge (*SI Appendix*, Section IV and Fig. S9). This analysis yields the relation

$$\tan^2\phi = \frac{\tan\phi_0 + \zeta}{1/\tan\phi_0 - \zeta} \quad [3]$$

between the leading angle ϕ and friction, where $\zeta = (F_{\mathrm{e},\theta\theta})\eta v_{\mathrm{b}}/G_{\mathrm{b}}$ denotes the scaled friction normalized by the biofilm shear modulus G_{b} and $F_{\mathrm{e},\theta\theta}$ describes the circumferential compression at the biofilm edge. In the absence of friction, i.e., when $\zeta = 0$, Eq. **3** reduces to $\phi = \phi_0$. In the presence of friction, our analysis predicts that the leading angle ϕ increases with ζ when $\zeta < 1/\tan\phi_0$, while the biofilm edge bulges out and constantly tumbles (no steady-state translation) if $\zeta > 1/\tan\phi_0$.

The experimental difficulty in measuring the friction coefficient η and the circumferential compression $F_{\mathrm{e},\theta\theta}$ precludes a direct quantitative comparison with theory; nevertheless, it is

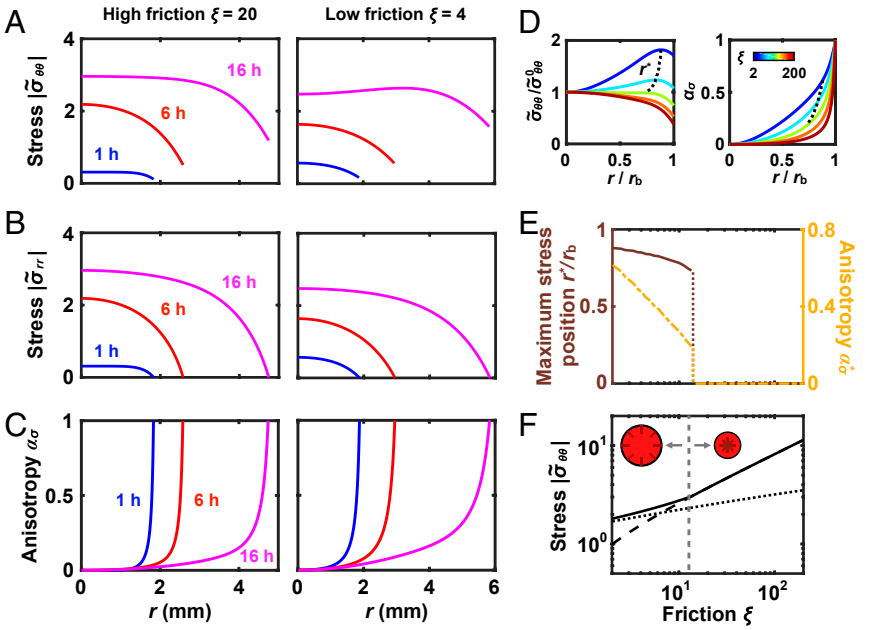

Fig. 3. Spatiotemporal evolution of the stress field in a growing biofilm. (*A–C*) Magnitude of (*A*) the circumferential stress $\tilde{\sigma}_{\theta\theta}$, (*B*) the radial stress $\tilde{\sigma}_{rr}$, and (*C*) the stress anisotropy $\alpha_\sigma = (\tilde{\sigma}_{\theta\theta} - \tilde{\sigma}_{rr})/(\tilde{\sigma}_{\theta\theta} + \tilde{\sigma}_{rr})$, plotted against the radial coordinate r at the designated times for high friction (*Left*; $\xi = 20$) and low friction (*Right*; $\xi = 4$). All of the stresses are normalized by the biofilm shear modulus G_b, i.e., $\tilde{\sigma} = \sigma/G_b$. Identical simulation parameters were used as in Fig. 2 *C* and *D*. (*D*) Circumferential stress $\tilde{\sigma}_{\theta\theta}$ (*Left*; normalized by the stress at the center of the biofilm $\tilde{\sigma}^0_{\theta\theta}$) and stress anisotropy α_σ (*Right*) versus the radial coordinate r normalized by the biofilm radius r_b plotted for different dimensionless friction parameters, defined as $\xi = \frac{\eta(k_g^{\max} R_{b0})}{G_b(H/R_{b0})}$, where η denotes the friction coefficient, $k_g^{\max}$ denotes the maximum growth rate of the biofilm, and R_{b0} and H denote the initial biofilm radius and thickness, respectively. Color scale indicates the values of ξ on a logarithmic scale. The five curves (colored from blue to red) correspond to $\xi = e^{0.7}$, $e^{1.7}$, $e^{2.7}$, $e^{3.7}$, and $e^{4.7}$, respectively. r^* denotes the radial position where the circumferential compressive stress reaches a maximum (black dotted curves). (*E*) The normalized radial coordinate r^*/r_b and the stress anisotropy α^*_σ at the position of maximum circumferential compressive stress, plotted as functions of the dimensionless friction parameter ξ. (*F*) The magnitude of the largest circumferential compressive stress $\tilde{\sigma}^*_{\theta\theta}$ ($r = r^*$; solid curve) compared to the circumferential stress at the edge ($r = r_b$; dotted curve) and at the center ($r = 0$; dashed curve) for different dimensionless friction parameters ξ. When the circumferential stress at the edge of the biofilm is larger (smaller) than the circumferential stress at the center, radial patterns start forming near the edge (near the center) as indicated by *Insets*. In experiments, the transition between two different morphologies occurs at 0.7% agar concentration (gray dashed line). (*D–F*) Simulation results at time t = 30 h, which is roughly when the experimental biofilms start to form periodic wrinkles.

clear from the measured ϕ of experimental biofilms that higher friction (i.e., higher concentration agar) increases the biofilm leading angle (*Materials and Methods*, Fig. 2*E*, and *SI Appendix*, Fig. S9).

Nonuniform Biofilm Growth Results in Anisotropic Stress. The evolution of mechanical stresses during the early stages of biofilm growth dictates the onset of mechanical instability and the consequent morphology of the wrinkles. Thus, we investigate the evolution of the magnitude of radial stress σ_{rr}, the magnitude of circumferential/hoop stress $\sigma_{\theta\theta}$, and the stress anisotropy defined as $\alpha_\sigma = (\sigma_{\theta\theta} - \sigma_{rr})/(\sigma_{\theta\theta} + \sigma_{rr})$ (59). The isotropic stress state corresponds to $\alpha_\sigma = 0$, while pure hoop stress corresponds to $\alpha_\sigma = +1$, and pure radial stress corresponds to $\alpha_\sigma = -1$.

The spatial distributions of stresses have distinctive characteristics during each of the three kinematic stages of biofilm expansion. Initially, the inner core of the biofilm only minimally expands ($\mathbf{F}^0_{e,\|} \cdot \mathbf{F}_{g,\|} \approx \mathbf{I}_\|$), which, given the material growth of the biofilm, $\mathbf{F}_{g,\|} = \lambda_g \mathbf{I}_\|$, must result in a compensating isotropic in-plane deformation ($\mathbf{F}^0_{e,\|} \approx \lambda_g^{-1} \mathbf{I}_\|$) and thus an isotropic compressive stress state with $\sigma_{rr} = \sigma_{\theta\theta}$ (Fig. 3 *A–C*). Moreover, stresses are approximately uniform in magnitude throughout the immobile core region of the biofilm but decline in the outer mobile region. Note that the value of radial stress σ_{rr} necessarily decreases to zero at the edge of the biofilm, while the hoop stress $\sigma_{\theta\theta}$ can be nonzero. Therefore, the stress anisotropy is initially localized to the outer mobile region.

As the biofilm continues to grow, internal stresses increase exponentially in time and eventually overcome friction, enabling the entire biofilm to expand uniformly (Figs. 2*D* and 3 *A–C*). During this second stage, mechanical stresses continue to increase exponentially and acquire a characteristic parabolic profile (Fig. 3 and *SI Appendix*, Section III). During the third stage when nutrients become depleted, stresses increase more slowly near the center of the biofilm due to the reduced rate of biofilm growth, while the magnitude of hoop stress near the edge still increases exponentially due to continuous biofilm growth in this nutrient-rich region (Fig. 2*C* and *SI Appendix*, Section III). As a result, when friction is low, the location of the maximum hoop stress shifts away from the center of the biofilm during the later stages (Fig. 3*A*). Note that the stress anisotropy is always positive (Fig. 3*C*), meaning that the compressive hoop stress is always larger in magnitude than the radial stress.

We found that the region of the biofilm under anisotropic stress becomes larger during the third stage of development (Fig. 3*C*). Thus, we hypothesized that the nonuniform growth pattern due to depletion of nutrients plays an important role in generating anisotropic stresses. To quantify the extent of stress anisotropy for the entire biofilm, we computed the normalized range of anisotropy $\Delta r_\alpha/r_b$, defined as the radial range of the area where $\alpha_\sigma > 0.1$ relative to the biofilm radius r_b, as a function of time. According to our model, the increase of $\Delta r_\alpha/r_b$ is accompanied by a narrowing of the nutrient-rich zone (*SI Appendix*, Fig. S10). To further explore this connection, we also computed the normalized anisotropy range for a

uniformly growing biofilm, which we found to be close to zero (*SI Appendix*, Fig. S10). We conclude that the faster growth at the biofilm edge promotes predominantly circumferential stress (*SI Appendix*, Section V), which explains the appearance of radial wrinkles in the peripheral regions in the experiments (Fig. 1*A*).

Friction Favors Isotropic Stress and Shifts the Position of Maximal Circumferential Stress. How does friction affect the distribution of mechanical stresses in a growing biofilm? To address this question, we compared the distribution of circumferential stress $\sigma_{\theta\theta}$ and stress anisotropy α_σ for a series of simulations with different friction coefficients (Fig. 3*D*). Notably, at a typical time when biofilms start to form patterns in experiments, our simulations show that the radial position r^*, corresponding to the maximal circumferential compressive stress, varies with the magnitude of friction: r^* is near the biofilm edge when friction is small, while r^* is at the biofilm center when friction is large (Fig. 3 *D* and *E*). Moreover, the stress anisotropy α_σ^* at r^* decreases toward zero (isotropic stress state) with increasing friction (Fig. 3 *D* and *E*).

Intuitively, these differences in stress distribution result from the counteracting effects of friction and nonuniform growth. Friction impedes biofilm expansion ($\mathbf{F}_\parallel \to \mathbf{I}_\parallel$ when $\eta \to \infty$), retards the relaxation of growth-induced isotropic compression ($\mathbf{F}^0_{e,\parallel} \to \lambda_g^{-1}\mathbf{I}_\parallel$ when $\eta \to \infty$), and thus favors isotropic stress in the biofilm center. By contrast, nonuniform growth favors peripheral circumferential stress due to the mismatch between the biofilm perimeter that increases only linearly in time and the exponential material growth of the biofilm at the edge. The fact that when friction is small, the circumferential stress close to the biofilm rim is larger than that at the center (Fig. 3 *D* and *F*) explains why, in experiments, the wrinkle pattern emerges from the outer region (Fig. 1 *A* and *B*). In contrast, in experiments with high concentration agar, the wrinkle pattern first appears in the center of the biofilm because the large friction results in strong isotropic compression in that region.

The In-Plane Stress Field Determines the Morphology of Biofilm Wrinkle Patterns. Last, we address how the stress profiles discussed above dictate the morphology of biofilm wrinkles. As the biofilm grows, the magnitude of compressive stresses increases (Fig. 3). Once compressive stresses reach a critical value σ_c, the flat state becomes unstable to the formation of wrinkles (26, 60, 61). When the biofilm shear modulus G_b is much larger than the agar shear modulus G_s, the critical compressive stress scales as $\sigma_c \sim G_s^{2/3} G_b^{1/3}$, and σ_c increases with $G_s (\propto \xi)$ in general (see *Materials and Methods* and ref. 26 for details). It was previously shown that for highly anisotropic stresses, wrinkles are oriented orthogonal to the direction of maximum compressive stress, whereas for isotropic stresses, wrinkles form zigzag herringbone-like patterns (60–65) (*SI Appendix*, Fig. S11). The stress profiles in Fig. 3 are thus consistent with the experimental observations in Fig. 1*A* that radial wrinkles form in the outer regions, where the stress is predominantly circumferential, whereas zigzag wrinkles form in the core region where the stress is largely isotropic.

In order to more quantitatively understand the spatiotemporal evolution of biofilm wrinkle patterns, we developed a 2D coarse-grained model that employs two scalar order parameter fields $\tilde{A}$ and $\tilde{S}$ to describe the amplitude and the shape of the wrinkle patterns, respectively. Specifically, $\tilde{A} = 0$ ($\tilde{A} > 0$) corresponds to the flat (wrinkled) state, and $\tilde{S} = 0$ ($\tilde{S} > 0$) corresponds to striped (zigzag) wrinkles. The total elastic deformation of a biofilm $\mathbf{F}_e = \mathbf{F}_e^w \cdot \mathbf{F}_e^0$ is decomposed as the superposition of the wrinkling deformation $\mathbf{F}_e^w$, which also deforms the agar, and the planar compression $\mathbf{F}_e^0$ (Fig. 4*A*). We follow previous work (60, 61) to describe wrinkles of different morphologies, and we use the herringbone ansatz to approximate the out-of-plane displacement in coarse-grained patches of the biofilm (Fig. 4*B* and *SI Appendix*, Section VI). The primary sinusoidal wrinkling with amplitude A_w (in the vertical z direction) and wavelength $\lambda_w = 2\pi/k_w$ occurs along the direction that corresponds to the maximum compressive stress (circumferential direction $\mathbf{e}_\theta$ in our case). The secondary sinusoidal wiggles with amplitude A_p (in the horizontal direction) and wavelength $\lambda_p = 2\pi/k_p$ appear in the orthogonal direction (Fig. 4*B*). In terms of these quantities, the relevant dimensionless order parameters are $\tilde{A} = k_w A_w$ and $\tilde{S} = k_p A_p/\sqrt{6}$.

The formation of wrinkles relaxes the elastic compressional energy of the biofilm but at the expense of the bending energy of the biofilm and the elastic deformation energy of the agar. By taking into account these energy contributions and using the above ansatz for the shape of wrinkles, we derived the following total free-energy density per unit area (*SI Appendix*, Section VI):

$$\frac{\Psi_\parallel^{\text{total}}}{G_b H} \approx -\frac{1}{4}\left((|\tilde{\sigma}^0_{\theta\theta}| - \tilde{\sigma}_c)(1 + 3b\tilde{S}^2) + 3(|\tilde{\sigma}^0_{rr}| - \tilde{\sigma}_c)\tilde{S}^2\right)\tilde{A}^2 + \frac{1}{8}\left(1 + (6b+3)\tilde{S}^2\right)\tilde{A}^4, \quad [4]$$

which is valid for stresses near the critical stress $\tilde{\sigma}_c = (3G_s/G_b)^{2/3}$ of the wrinkling instability. Here stresses $\tilde{\sigma} \equiv \sigma/G_b$ are normalized by the biofilm shear modulus G_b. $\tilde{\sigma}^0_{\theta\theta} < 0$ and $\tilde{\sigma}^0_{rr} < 0$ denote the circumferential and radial prestress, respectively, due to the planar compression $\mathbf{F}_e^0$. We set $b \approx 2/3$ to ensure that the relaxed stresses due to wrinkling remain isotropic when the imposed prestress is isotropic (*SI Appendix*, Section VI).

Here we assume that the dynamics of wrinkling is determined by the slower dynamics of the stress field. Under this approximation, the predicted wrinkled morphology corresponds to the minimum of the free energy in Eq. **4**. The wrinkling instability occurs via two successive continuous phase transitions controlled by the magnitude and by the anisotropy of the prestress (*SI Appendix*, Section VI and Fig. S11). The primary bifurcation from the planar state ($\tilde{A} = 0$) to the wrinkled state ($\tilde{A} > 0$) occurs if the magnitude of the maximum compressive stress $|\tilde{\sigma}^0_{\theta\theta}|$ exceeds the critical value $\tilde{\sigma}_c$, while a secondary bifurcation from striped wrinkles ($\tilde{S} = 0$) to zigzag wrinkles ($\tilde{S} > 0$) occurs only when the stress anisotropy is sufficiently small, $\alpha^0_\sigma < (|\tilde{\sigma}^0_{\theta\theta}| - \tilde{\sigma}_c)/(3|\tilde{\sigma}^0_{\theta\theta}| + \tilde{\sigma}_c)$. Note that for isotropic compressive prestresses ($\tilde{\sigma}^0_{\theta\theta} = \tilde{\sigma}^0_{rr}$) the free-energy density is minimized by $\tilde{S} = 1$.

The Evolution of the Stress Field Determines the Biofilm Wrinkling Morphodynamics. Wrinkling relaxes the mechanical stresses in the biofilm by releasing the in-plane compressive strain through out-of-plane deformation. Once wrinkling occurs, this relaxation mechanism prevents compressive stresses from increasing beyond the critical stress (*Materials and Methods* and *SI Appendix*, Section VI and Fig. S11).

We incorporated the above mean-field adiabatic description of the wrinkling instability and consequent stress relaxation into our chemomechanical model (see *Materials and Methods* and *SI Appendix*, Section VI, for details). Consistent with the experimental observations in Fig. 1*B*, we find that for biofilms grown on low-concentration agar (low shear modulus of the substrate and small friction since we assume $\eta \propto G_s$), radial wrinkles initiate near the outer edge, then propagate inward, and once they reach the center, zigzag wrinkles form in the core region (Figs. 1*B* and 4*C*). On the other hand, for biofilms grown on high-concentration agar (high shear modulus of the substrate and large friction), radial wrinkles initiate in the center and expand outward, while zigzag wrinkles simultaneously appear in the core region (Figs. 1*B* and 4*D*). According to our model, compared to

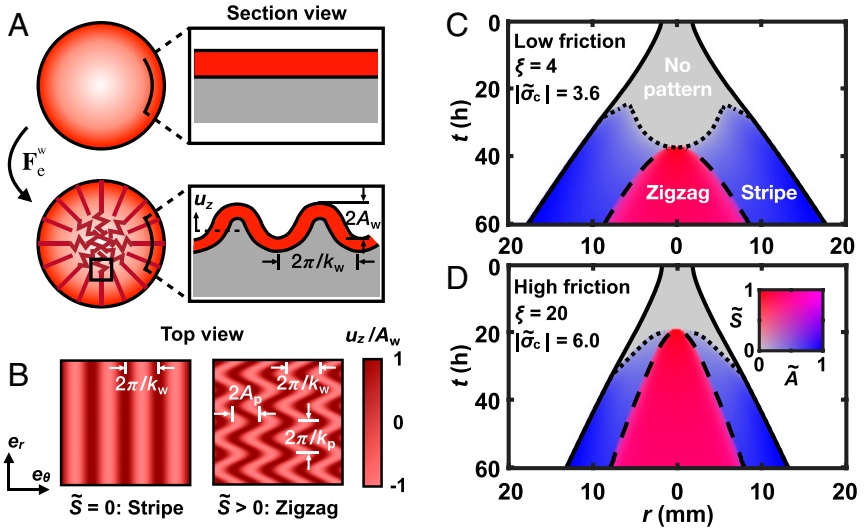

Fig. 4. Morphology and spatiotemporal dynamics of biofilm wrinkle patterns. (*A* and *B*) Schematic of the wrinkling model. The wrinkling deformation tensor, denoted by $\mathbf{F}_e^w$, maps a prestressed, flat biofilm (*Top*) to a wrinkled biofilm (*Bottom*). Color code as in Fig. 2*B*. The wrinkling pattern is characterized by two dimensionless scalar fields: the normalized amplitude $\tilde{A}$ and the shape factor $\tilde{S}$. $\tilde{A}$ is defined as the product of the wave number (denoted by k_w) and the amplitude (denoted by A_w) of periodic wrinkles. $\tilde{S} = k_p A_p/\sqrt{6}$, where k_p and A_p denote the wave number and the amplitude, respectively, of in-plane wiggles. The shape parameter $\tilde{S}$ was normalized such that its values are restricted to the interval [0, 1]. (*A*, *Right*) Close-up cross-sections of a flat ($\tilde{A} = 0$) and a wrinkled ($\tilde{A} > 0$) biofilm. u_z denotes the out-of-plane displacement. *B* shows top view schematics of the herringbone ansatz, $u_z = A_w \cos[k_w(x_\theta - A_p \cos k_p x_r)]$, for a straight striped pattern ($\tilde{S} = 0$) and a zigzag pattern ($\tilde{S} > 0$). Here $x_\theta = r\theta$ and $x_r = r$ denote the linear coordinates along the circumferential and radial directions, respectively. (*C* and *D*) Kymograph representation of the evolution of patterns of the modeled biofilm for designated parameters ($\tilde{\sigma}_c$ denotes the critical stress, normalized by the biofilm modulus G_b, for the onset of the wrinkling instability). The top and bottom kymographs can be interpreted as biofilms grown on different agar concentrations (Fig. 1*B*). $\tilde{\sigma}_c$ in *C* is chosen such that the wrinkling instability occurs at a time similar to that in experiment. $\tilde{\sigma}_c$ in *D* is then inferred according to the dependence of critical stress on $G_s/G_b \propto \xi$. See *Materials and Methods* for details. Solid, dotted, and dashed curves denote the boundaries of the entire biofilm, regions with a radial stripe pattern ($\tilde{A} > 0, \tilde{S} = 0$), and regions with a zigzag pattern ($\tilde{A} > 0, \tilde{S} > 0$), respectively. Gray denotes the region without any pattern. For the patterned regions, the color of each spatiotemporal bin indicates the local amplitude $\tilde{A}(r, t)$ and shape $\tilde{S}(r, t)$ of the pattern. The color code is shown in *D*, *Inset*.

the case where the wrinkling instability is prevented, the expansion of the wrinkled biofilm is slowed, the stress anisotropy is reduced, and the magnitude of compressive stress is reduced as well (*SI Appendix*, Figs. S11 and S12). Thus, our model suggests that wrinkling due to a growth-induced mechanical instability feeds back and further influences biofilm expansion and pattern formation by modifying the distribution of internal stress.

Discussion

Biofilm formation has been shown to protect the resident bacteria from a wide range of environmental challenges, including phagocytosis, antibiotics, and physical perturbations (18). Because they are so tenacious, biofilms pose serious problems in clinical infections as well as in contamination of industrial facilities and medical devices. Our major findings concern how mechanical interaction between a biofilm and its substrate influences biofilm expansion and wrinkling. In particular, we found that surface friction gives rise to distinct kinematic stages of biofilm expansion and that the spatiotemporal wrinkling patterns can be altered by varying the magnitude of this friction. Our results may thus provide insights into new strategies to restrict biofilm spreading by manipulating the mechanical interaction with the substrate.

Our experimental and modeling results highlight the connections between nutrient supply, bacterial growth, biofilm and substrate mechanics, and friction in shaping the morphology of developing bacterial biofilms on soft substrates. The depletion of nutrients beneath the center of the biofilm leads to localized growth primarily near the biofilm edge, consistent with previous experiments (25, 26, 39–42). This uneven growth profile, in turn, produces compressive stresses, which are predominantly circumferential at the periphery of the biofilm but are largely isotropic in the central region. The consequence of such a stress profile is the formation of radial wrinkles in the outer region of the biofilm and a zigzag herringbone-like pattern in the central region. Moreover, the location of the maximum circumferential compressive stress—where wrinkles first appear once the magnitude of the stress reaches a critical value—varies with the magnitude of friction, from near the outer edge when friction is small to near the center when friction is large. As a result, for biofilms grown on soft agar substrates with low friction, wrinkles first appear in the peripheral region and propagate inward. In contrast, for biofilms grown on stiff agar substrates with high friction, wrinkles first appear in the central region and propagate outward.

What are the biological implications of forming 3D biofilm structures? One notion concerns the possibility of a mechanical mode of bacterial infection as it was recently shown that *V. cholerae* biofilms could mechanically deform and damage epithelia (66). Another possibility is that the wrinkled thin film structure provides a larger surface area-to-volume ratio compared to a flat film, thereby enhancing access to nutrients and conferring growth advantages to the bacterial population (38, 67). The convoluted 3D structure of biofilms also brings distant cells closer compared to a flat film of the same area, which might enhance communication between bacterial cells, e.g., via quorum-sensing signaling (68, 69). Finally, the 3D biofilm structure positions biofilm cells at different heights, potentially generating a "bet hedging" strategy under particular conditions. For example, the rough surfaces of wrinkled biofilms exposed to external flows will alter the flow field, forming large (small) shear stress zone near the peaks (valleys) of wrinkles. Consequently, the cells near the peaks will exhibit a larger probability to detach, while the cells near the valleys will tend to stay attached to the surfaces (70).

Our results provide insight into the spatiotemporal development of *V. cholerae* biofilm morphology, but it remains to

be explored whether and how the increasing mechanical stress and/or the formation of the 3D biofilm structure affect the proliferation rate of bacteria, alter biofilm matrix production, or promote survival success of cells in particular biofilm regions. Additional experimental studies will be required to complete our understanding of how growth, mechanical stresses, and morphological transitions are coupled to drive biofilm development. Furthermore, our study focused only on the initial stages of wrinkling, during which the amplitudes of wrinkles are small and biofilms remain in contact with the agar substrate. We previously demonstrated that at later stages of development, biofilms can locally delaminate from the agar substrate, which significantly influences the subsequent development of morphological patterns (26).

In this work, we modeled the rheology of growing *V. cholerae* biofilms as that of a hyperelastic material. However, our previous measurements show that *V. cholerae* biofilms actually behave as more complex viscoelastic media that yield upon large shear deformation (36). Indeed, our elastic material model leads to stresses that are larger than the measured yield stress. We thus suspect that yielding constantly occurs during *V. cholerae* biofilm growth. More generally, reorganization and yielding of growing biological materials are commonly observed during morphogenesis, for example, in plants (71), fruit flies (72, 73), and brain tissues (74). Thus, the effects of viscoelasticity (75) and elastoplasticity (*SI Appendix*, Figs. S13 and S14) of biofilms on their morphological development will be an important topic for future studies.

The concepts we presented here to analyze the development of *V. cholerae* biofilms should also be applicable to biofilms of many other bacterial species that form similar morphological patterns (76–78). However, there are also examples of biofilms with distinct morphologies, such as the distorted concentric rings observed in wild-type *P. aeruginosa* PA14 biofilms (43) and biofilms formed by *E. coli* K-12 strain W3110 (21). Our model suggests that if biofilm growth and/or matrix production is faster in the central region than the outer region, one expects a region in which the radial compressive stress surpasses the circumferential stress. In this case, our model predicts that wrinkles will form as concentric (possibly distorted) rings (*SI Appendix*, Fig. S11). Such a pattern of matrix production is indeed reported in the two biofilm formers mentioned above. For example, in wild-type *P. aeruginosa* PA14 biofilms, cells at the biofilm center display upregulated matrix production due to oxygen limitation, whereas cells located in the oxygen-rich periphery down-regulate matrix production (43). In biofilms formed by *E. coli* K-12 strain W3110, cells generate matrix components (amyloid curli fibers) only upon entry into stationary phase when nutrients are depleted, which typically occurs first at the biofilm center (21). Thus, we expect that similar physical mechanisms to those underlying the dynamics of expansion and pattern formation of *V. cholerae* biofilms may be widely applicable to other bacterial biofilms, including those with distinct morphologies. Our findings also provide a window into how patterns might form dynamically in higher systems that are less tractable to genetic or physical manipulation.

Materials and Methods

Growing and Imaging Experimental Biofilms.

Bacterial strain and biofilm growth. The *V. cholerae* strain used in this study is a derivative of the *V. cholerae* O1 biovar El Tor strain C6706str2 (79) that harbors a missense mutation in the *vpvC* gene (VpvC W240R), which elevates the levels of c-di-GMP and confers a rugose biofilm phenotype (80). Standard lysogeny broth (LB) medium solidified with different percentages of agar was used as the solid support on which biofilms were grown. Initially, *V. cholerae* was streaked onto LB plates containing 1.5% agar and grown at 37 °C overnight. Individual colonies were selected and inoculated into 3 mL of LB liquid medium containing ∼10 glass beads (MP Biomedicals Roll and Grow Plating Beads, 4 mm diameter), and these cultures were then grown at 37 °C with shaking to midexponential phase (about 5 h). Subsequently, the cultures of bacteria were mixed by vortex to break clumps up into individual cells, the OD_{600} was measured with a cell density meter (Amersham Biosciences Ultrospec 10), and then the cultures were diluted back to an OD_{600} value of 0.5. One microliter of these preparations was spotted onto prewarmed agar plates made with different concentrations of agar. Subsequently, the plates were incubated at 37 °C. During the first 10 h after inoculation, bacterial colonies formed the initial biofilms without extending beyond the inoculated circle (radius $R_{b0} \approx 2$ mm). These biofilms were used as the initial/reference configurations for modeling, with $t = 0$ in our simulations corresponding to the time when a biofilm starts expanding radially. Four biofilms were grown per agar plate for the surface topography measurements, while for the time-lapse imaging, one biofilm was grown on each agar plate.

Time-lapse transmission imaging. The imaging system has been described previously (26). Briefly, an agar plate containing the inoculum was placed on an LED illumination pad (Huion L4S Light Box) and imaged with a Nikon D3300 SLR camera equipped with a Sigma 105-mm F2.8 Macro Lens. The entire setup was placed in a 37 °C environmental room and was covered to exclude light. The camera was controlled with DigiCamControl software. Imaging started 5 h after inoculation when the camera was capable of focusing on the growing biofilms. Image snapshots were taken automatically every 15 min for 3 d.

Image processing. The protocol and MATLAB codes used to analyze the morphological features of biofilms have been reported previously (26). In brief, an intensity-based thresholding method was used to binarize the preprocessed transmission images (using a built-in thresholding function in MATLAB) and to separate the biofilm region from the background. For each biofilm, the transmission image taken 12 h after inoculation was used to define the biofilm center for the entire time course. The biofilm radius r_b was computed by averaging the distance between each point on the circumference and the center.

Regions of the biofilm were binned into rings of width 0.2 mm for further analysis. First, we took the Fourier transform of the image intensity in the circumferential direction for each separate ring at distance r from the center of the biofilm. Radial stripes appear in the resulting power spectrum as a sharp maximum at nonzero spatial frequency $f(r, t)$. The radial coordinate, at which the peak power instead appears at zero spatial frequency, was defined as the boundary of the region with a radial stripe pattern. Next, the radial intensity distribution $I(r)$ was obtained by averaging the intensity values over the circumferential direction for each ring. The intensity $I(r)$ for the disordered core is distinctly different (darker) from that of the outer region of the biofilm. Thus, we set a threshold intensity value for each biofilm to identify the central region with a disordered zigzag pattern, enabling us to measure this central region's radius as a function of time.

The velocity field of an expanding biofilm was measured by particle image velocimetry (PIV) performed with the open source tool PIVlab (81). The 2D displacement field between two successive frames (separated by 30 min) was computed via a Fourier transform correlation with three passes. The sizes of interrogation windows for the three passes were chosen to be 128, 64, and 32 pixels. By averaging the radial components of the coarse-grained velocity vectors over the circumferential direction for each ring, we obtained the radial velocity field in Fig. 2*D*. Error bands correspond to standard deviations of the means.

Three-dimensional confocal profiling and leading angle measurement. The surface profiles of biofilms grown for different times were analyzed with a Leica DCM 3D Microoptical System. A 10× objective was used to image a roughly 3 mm × 3 mm region of the biofilm, with a step size of 2 μm in the z direction. Subsequent processing and analyses were performed using Leica Map software. First, the three-point flattening procedure was performed on the agar surface to level the image. Three-dimensional views of biofilms were then rendered with a built-in function in the software.

To measure the leading angle of an expanding biofilm, line profiles perpendicular to the biofilm periphery and spanning the region from the agar surface to the top surface of the biofilm were generated at five different locations. For each line profile, two points were manually selected on the biofilm edge, which were used to obtain a sloped line. The leading angle was then extracted with a built-in function in the software from the slope of this line. The measurements of the initial angle were performed 12 h after inoculation. The steady-state leading angles were measured every 4 h from 24 to 48 h after inoculation.

Modeling Biofilms.

Continuum modeling. To model the combined role of growth and mechanics in the morphological transition of *V. cholerae* biofilms, we adopted the

formulation of elastic growth (49, 50), where the total geometric stretches $\mathbf{F} = \partial \boldsymbol{x}/\partial \boldsymbol{X}_0$, defined as the deformation gradient from the initial configuration $\boldsymbol{X}_0$ to the current configuration $\boldsymbol{x}$, are decomposed into stretches $\mathbf{F}_g$ due to growth and stretches $\mathbf{F}_e$ due to elastic deformation. Below, we describe a 2D chemomechanical model of biofilm development that includes diffusion of nutrients and their uptake by bacteria, bacterial growth/extracellular matrix production, and mechanical deformation. The subscript $\parallel$ is used to denote the in-plane components of 3D vectors/tensors and reduced 2D variables, while a tilde ($\sim$) above a variable is used to denote a dimensionless variable.

Growth. Local growth of the *V. cholerae* biofilm is treated as horizontal isotropic growth, i.e., $\mathbf{F}_g = \begin{pmatrix} \lambda_g(t)\mathbf{I}_\parallel & \mathbf{0} \\ \mathbf{0} & 1 \end{pmatrix}$, where $\mathbf{I}_\parallel$ denotes the 2D identity matrix. $\lambda_g(t)$ describes the stretch in the horizontal direction due to growth, while there is no growth in the z direction because biofilms maintain approximately constant thickness. The stretch due to growth evolves as $\partial \lambda_g/\partial t = k_g \lambda_g$, where k_g denotes the local growth rate. To capture the nutrient-dependent spatially nonuniform growth, $k_g(\tilde{c}_\parallel)$ is assumed to be a function of the normalized 2D nutrient field $\tilde{c}_\parallel(\boldsymbol{x}_\parallel, t)$ (normalized by the concentration of nutrients c_0 at the edge of the biofilm, i.e., $\tilde{c}_\parallel(\boldsymbol{x}_\parallel, t) \equiv c_\parallel(\boldsymbol{x}_\parallel, t)/c_0$), which reflects the nutrient availability in the agar medium. The equation that describes diffusion and uptake of nutrients is $\partial_t \tilde{c}_\parallel = D\nabla_\parallel \tilde{c}_\parallel - Q(\mathbf{F}_e)\phi(\tilde{c}_\parallel) = Q_0(a_c^2 \nabla_\parallel \tilde{c}_\parallel - J_{e,\parallel}^{-1}\phi(\tilde{c}_\parallel))$, where D is the nutrient diffusion coefficient, Q_0 characterizes the maximum nutrient uptake rate by bacteria in the undeformed grown configuration, and $J_{e,\parallel} = \det(\mathbf{F}_{e,\parallel})$ is introduced to account for the increased areal density of bacterial cells upon elastic deformation of the biofilm. The characteristic width of the nutrient-rich annulus near the biofilm edge is given by $a_c = (D/Q_0)^{1/2}$. We assume that the uptake of nutrients depends on the local availability of nutrients via the Monod law, i.e., $\phi(\tilde{c}_\parallel) = \tilde{c}_\parallel/(\tilde{c}_\parallel + \tilde{K})$, where $\tilde{K} = 0.5$ is the concentration of nutrients at the half-maximal uptake rate (54) (note that our model results are insensitive to the specific choice of $\tilde{K}$: for a different $\tilde{K}$, a similar $\tilde{c}_\parallel$ profile can be obtained by adjusting the uptake rate Q_0; see below for the fitting procedure). Finally, the growth rate is specified as $k_g(\tilde{c}_\parallel) = k_0\phi(\tilde{c}_\parallel) + k_r$, where k_0 is the maximum rate of nutrient-dependent growth and a small, constant nutrient-independent growth rate k_r is added to account for the residual biofilm growth due to the vertical diffusion of nutrients (*SI Appendix*, Section II and Figs. S2 and S3).

Mechanics. The growth of the biofilm drives its expansion. As the biofilm moves relative to the agar, the friction $\boldsymbol{f}$ between the biofilm and the agar impedes biofilm expansion and induces internal mechanical stresses $\boldsymbol{\sigma}$. Friction is modeled as a viscous drag, i.e., $\boldsymbol{f} = -\eta \boldsymbol{v}_\parallel$, which is proportional to the expansion velocity of the biofilm $\boldsymbol{v}_\parallel = (\partial \boldsymbol{x}_\parallel/\partial t)_{\boldsymbol{x}_0}$, and the drag coefficient η is assumed to be proportional to the agar shear modulus G_s (56–58, 82, 83) (*SI Appendix*, Section IIG and Fig. S5). In order to relate stress $\boldsymbol{\sigma}$ to elastic deformation $\mathbf{F}_e$, we leverage the fact that the thickness of the biofilm ($\sim 100\ \mu$m) is always about 10 to 100 times smaller than its radius ($\gtrapprox 5$ mm), and we treat the biofilm as a plane stress thin film made from nearly incompressible hyperelastic material. Thus, the thin-film deformation $\mathbf{F}_e = \mathbf{F}_e^w \cdot \mathbf{F}_e^0$ is decomposed into the product of a wrinkling deformation $\mathbf{F}_e^w$ and a planar deformation $\mathbf{F}_e^0 = \begin{pmatrix} \mathbf{F}_{e,\parallel}^0 & \mathbf{0} \\ \mathbf{0} & \gamma^0 \end{pmatrix}$, where $\mathbf{F}_{e,\parallel}^0$ denotes the in-plane compression and γ^0 denotes the resulting vertical stretch. Lateral force balance yields $\eta q \boldsymbol{v}_\parallel = H\nabla_\parallel \cdot (\gamma^0 \boldsymbol{\sigma}_\parallel)$, where H denotes biofilm thickness in the undeformed configuration, and $q = q(\mathbf{F}_e^w)$ is a factor that accounts for the increase of the contact area between the biofilm and the agar due to the wrinkling profile.

Prior to wrinkling, the biofilm is flat, and thus, $\mathbf{F}_e^w = \mathbf{I}$ and $q = 1$. The deformation $\mathbf{F}_e^0$ can be obtained from $\mathbf{F}_{e,\parallel}^0 = \partial \boldsymbol{x}_\parallel/\partial \boldsymbol{X}_{0,\parallel}$ and from $\gamma^0 = 1/\det(\mathbf{F}_{e,\parallel}^0)$ due to incompressibility. The in-plane stresses are calculated to be $\boldsymbol{\sigma}_\parallel^0 = G_b[\mathbf{F}_{e,\parallel}^0 \cdot (\mathbf{F}_{e,\parallel}^0)^T - (\gamma^0)^2 \mathbf{I}_\parallel]$, where G_b denotes the biofilm shear modulus (see *SI Appendix*, Sections I and II, for details). A wrinkling instability occurs once compressive stresses reach the critical value. To describe the wrinkling deformation $\mathbf{F}_e^w$ we use two coarse-grained scalar fields, the amplitude $\tilde{A}$ and the shape $\tilde{S}$ (Fig. 4 and *SI Appendix*, Section VI). The fields $\tilde{A}$ and $\tilde{S}$ are computed from a Landau–Ginzburg-type free energy density (Eq. **4**), and the factor q is approximated as $q(\tilde{A}, \tilde{S}) = 1 + \frac{1}{4}\tilde{A}^2[1 + 3(b+1)\tilde{S}^2]$, where $b \approx 2/3$ (see *SI Appendix*, Section VI, for details). The stress relaxation from the prestress $\boldsymbol{\sigma}_\parallel^0$ to the true stress $\boldsymbol{\sigma}_\parallel$ due to wrinkling is described by (*SI Appendix*, Section VI)

$$\begin{aligned} \sigma_{\theta\theta} &\approx \sigma_{\theta\theta}^0 + \tilde{A}^2\left[1 + (3b + 3/2)\tilde{S}^2\right]G_b, \\ \tilde{\sigma}_{rr} &\approx \sigma_{rr}^0 + \tilde{A}^2\left[1/2 + (3b/2 + 3)\tilde{S}^2\right]G_b. \end{aligned} \quad [5]$$

Note that for isotropic compressive prestresses ($\sigma_{\theta\theta}^0 = \sigma_{rr}^0$), the relaxed stresses remain isotropic ($\tilde{S} = 1$), when $b = 2/3$.

Dimensionless governing equations. We define dimensionless variables $\tilde{\boldsymbol{\sigma}} = \boldsymbol{\sigma}/G_b$, $\tilde{\boldsymbol{x}} = \boldsymbol{x}_\parallel/R_{b0}$, and $\tau = t/\tau_0$, where the shear modulus of the biofilm G_b was chosen as the scale for stresses, the initial biofilm radius R_{b0} as the characteristic length scale, and the inverse of the growth rate at the edge of the biofilm $\tau_0 = (k_g^{max})^{-1} = [k_g(r = r_b)]^{-1}$ as the characteristic time scale associated with biofilm expansion. Upon nondimensionalizing the equations describing biofilm growth and mechanics discussed above, we obtain the following equations:

$$\text{Nutrient diffusion and uptake: } \partial_\tau \tilde{c}_\parallel = \tilde{Q}_0\left[\tilde{a}_c^2 \tilde{\nabla}_\parallel^2 \tilde{c}_\parallel - J_{e,\parallel}^{-1}\phi(\tilde{c}_\parallel)\right], \quad [6a]$$

$$\text{Nutrient limited growth: } \partial_\tau \lambda_g = \left[\phi(1)^{-1}(1 - \tilde{k}_r)\phi(\tilde{c}_\parallel) + \tilde{k}_r\right]\lambda_g, \quad [6b]$$

$$\text{Force balance: } \tilde{\nabla}_\parallel \cdot (\gamma^0 \tilde{\boldsymbol{\sigma}}_\parallel) = \xi q(\tilde{A})\tilde{\boldsymbol{v}}_\parallel, \quad [6c]$$

$$\text{Constitutive relation: } \tilde{\boldsymbol{\sigma}}_\parallel^0 = \mathbf{F}_{e,\parallel}^0 \cdot (\mathbf{F}_{e,\parallel}^0)^T - (\gamma^0)^2 \mathbf{I}_\parallel, \quad [6d]$$

where $\tilde{Q}_0 = Q_0\tau_0$, $\tilde{k}_r = k_r\tau_0$, and the dimensionless friction $\xi = \frac{\eta(R_{b0}/\tau_0)}{G_b(H/R_{b0})}$ is identified to be a control parameter of the model. Before wrinkling occurs, $\tilde{\boldsymbol{\sigma}}_\parallel = \tilde{\boldsymbol{\sigma}}_\parallel^0$. After wrinkling occurs, Eq. **6d** describes the prestress $\tilde{\boldsymbol{\sigma}}_\parallel^0$, and the actual stress $\tilde{\boldsymbol{\sigma}}_\parallel$ is computed from Eq. **5**. Taken together, the set of dimensionless governing equations is able to describe both the planar expansion of the biofilm ($\tilde{A} = 0$) and the 3D biofilm wrinkling morphology ($\tilde{A} > 0$). The parameters in our model are either estimated directly from experiment or are obtained by fitting to experimental data (*SI Appendix*, Fig. S1 and Table S2).

Numerical simulations. The numerical solutions of Eq. **6** were obtained by performing finite element simulations. Rather than solving Eqs. **6a** and **6c** in the Eulerian frame, these equations were rewritten and solved in the Lagrangian frame of reference (see *SI Appendix*, Section IID, for details). We further assumed axisymmetric solutions and expressed the governing equations in polar coordinates to numerically solve for six scalar fields $\tilde{r}$, λ_g, $\tilde{c}_\parallel$, $\tilde{\gamma}$, $\tilde{A}$, and $\tilde{S}$ as functions of the dimensionless initial radial coordinate $\tilde{R}_0$. The validity of the axisymmetry assumption was verified by comparing to simulations on 2D circular domains with no assumption of symmetry. We used a fixed 1D domain of $\tilde{R}_0 \in [0, 1]$ that was discretized and generated by Gmsh (84). The geometric stretch near the edge $\tilde{R}_0 = 1$ is larger than that near the center $\tilde{R}_0 = 0$ due to the nonuniform growth. Therefore, we used a finer discretization of the domain near $\tilde{R}_0 = 1$ to ensure high-precision numerical solutions.

The initial conditions are $\tilde{r}(\tilde{R}_0, \tau = 0) = \tilde{R}_0$, $\tilde{c}_\parallel(\tilde{R}_0, \tau = 0) \equiv 1$, $\lambda_g(\tilde{R}_0, \tau = 0) \equiv 1$, $\gamma^0(\tilde{R}_0, \tau = 0) \equiv 1$, $\tilde{A}(\tilde{R}_0, \tau = 0) = \tilde{S}(\tilde{R}_0, \tau = 0) \equiv 0$, with boundary conditions $\tilde{c}_\parallel(\tilde{R}_0 = 1, \tau) = 1$, $\tilde{\sigma}_{rr}(\tilde{R}_0 = 1, \tau) = 0$. Partial differential equations were then converted to their equivalent weak forms and computationally discretized by first-order (two-noded) linear elements (85), and implemented in the open-source computing platform FEniCS (86). The time increment was set to be $\Delta\tau = 0.01$. At each time step, we used the standard Crank–Nicolson method to perform the numerical integration (87). To ensure numerical convergence, we checked explicitly whether the wrinkling instability occurred by evaluating the difference between the circumferential stress and the critical stress $\delta_\sigma = |\tilde{\sigma}_{\theta\theta}^0| - \tilde{\sigma}_c$. We required that $\delta_\sigma^{(n)} > 0$ at $\tau = n\Delta\tau$ for the wrinkling to occur at $\tau = (n+1)\Delta\tau$.

Choice of parameters.

Critical stress for wrinkling. Our previous study revealed that a trilayer model quantitatively captures the biofilm wrinkle wavelength (26). The trilayer theory also predicts how the critical stress varies with the stiffness contrast between the biofilm and the substrate $G_s/G_b \propto \xi$ (88) (see also ref. 26 for the calculated values of critical stress and G_s/G_b for different agar concentrations). However, our chemomechanical model (Eq. **6**) reaches the theoretical critical stress earlier than the time when wrinkling occurs in the experiments because we model biofilms as elastic materials and do not consider viscoelasticity and plasticity (*Discussion* and *SI Appendix*, Section VII). In practice, we rescale the critical stress $\tilde{\sigma}_c$ in Fig. 4 *C* and *D* such that wrinkling instability in the simulations occurs at a time similar to that in experiment.

Fitting parameters from the velocity profiles. The dimensionless friction parameter ξ and the dimensionless maximum rate of nutrient uptake $\tilde{Q}_0$ were determined by fitting the radial velocity profiles of the modeled biofilm to those extracted from experiments at different times. The similarity between the radial velocity profiles was assessed in terms of the normalized mean squared distance (MSD). In experiments, we measured

the radial velocity profiles for a biofilm grown on 0.7% agar concentration at 40 different time points t_j separated by 30 min from $t = 0$ h to $t = 20$ h (before the wrinkling instability occurs) as described above in *Image processing*. At each time t_j, the experimental data were represented as $(\hat{r}_{i,j}, \hat{v}_{i,j})$ $(i = 1, \ldots, N_j$; $\hat{v}_{i,j}$ averaged over the circumferential direction). The number of data points N_j at each time point is equal to the ratio of the biofilm radius to the width of radial bins (32 pixels). For a particular set of parameters $(\xi, \tilde{Q}_0)$, we first numerically computed the velocity profiles $v(r, t_j)$ of the modeled biofilm. For each time point t_j we computed the normalized squared distance (SD) $\Delta\tilde{s}^2_{i,j}$ between the experimental data points $(\hat{r}_{i,j}, \hat{v}_{i,j})$ and the simulated profile $v(r, t_j)$ as $\Delta\tilde{s}^2_{i,j} = \min_r \left\{ \left(\frac{\hat{r}_{i,j} - r}{L_0}\right)^2 + \left(\frac{\hat{v}_{i,j} - v(r,t_j)}{V_0}\right)^2 \right\}$ where we used a characteristic length scale $L_0 = 5$ mm and a characteristic velocity $V_0 = 3$ μm/min. The normalized SD between the radius and edge velocity for the experimental biofilm and those of the modeled biofilm was used as one additional data point $\Delta\tilde{s}^2_{N_j+1,j}$ associated with time t_j. Finally, the normalized MSD was calculated as $\frac{1}{(N_j+1)N_t} \sum_{j=1}^{N_t} \sum_{i=1}^{N_j+1} \Delta\tilde{s}^2_{i,j}$. We searched the parameter space to find the optimal parameter values ξ^* and $\tilde{Q}_0{}^*$ that minimize the normalized MSD (Fig. S1). For simulations with different friction, we varied the parameter ξ keeping all of the other parameters fixed.

Analysis of the biofilm leading angle. To compare the biofilm leading angles in experiments with theoretical predictions, we inferred the value of η/G_b for biofilms grown on 0.7% agar by fitting the velocity profiles as described above, i.e., $(\eta/G_b)^* = \frac{\xi^*(H/R_{b0})}{R_{b0}/\tau_0}$. Next, we inferred the normalized friction $(\eta/G_b)v_b$ for biofilms grown on different agar concentrations (agar shear modulus denoted by G_s) by making the assumption that $(\eta/G_b) \propto G_s/G_b$, i.e., $(\eta/G_b)v_b = (\eta/G_b)^* \times \frac{(G_s/G_b)}{(G_s/G_b)|_{\text{agar conc.} = 0.7\%}} \times v_b$. The uncertainty of these values (Fig. 2*E*, horizontal error bars) was estimated by taking into account the measurement errors of G_s, G_b, and v_b (these quantities were measured previously in refs. 26 and 36). The value of the circumferential compression $F_{e,\theta\theta}$ in Eq. **3** remains undetermined. Nevertheless, we can estimate $F_{e,\theta\theta} \in (0.7, 0.9)$ from the wrinkling instability analysis (26). The specific choice of $F_{e,\theta\theta}$ in this range only minimally affects the results (*SI Appendix*, Fig. S9).

Data and Software Availability. MATLAB codes for the image processing have been described in a previous publication (26). All data and simulation codes used in this paper are available to the readers on GitHub: https://github.com/f-chenyi/biofilm-mechanics-theory.

ACKNOWLEDGMENTS. This work was supported by the Howard Hughes Medical Institute (B.L.B.); NSF Grants MCB-1713731 (B.L.B.) and MCB-1853602 (B.L.B., H.A.S., and N.S.W.); NIH Grant 1R21AI144223 (B.L.B., H.A.S., and N.S.W.); NIH Grant 2R37GM065859 (B.L.B.); NIH Grant GM082938 (N.S.W.); the NSF through the Princeton University Materials Research Science and Engineering Center DMR-1420541 (B.L.B., H.A.S., and A.K.); and the Max Planck Society-Alexander von Humboldt Foundation (B.L.B.). J.Y. holds a Career Award at the Scientific Interface from the Burroughs Wellcome Fund. R.A. acknowledges support from the Human Frontiers of Science Program (LT-000475/2018-C). We thank Dr. Paola Nardinocchi, Dr. Maria Holland, Dr. Jie Yin, and Dr. Eleni Katifori for helpful discussions.

1. A. Goriely, *The Mathematics and Mechanics of Biological Growth* (Springer, 2017), vol. 45.
2. R. de Rooij, E. Kuhl, A physical multifield model predicts the development of volume and structure in the human brain. *J. Mech. Phys. Solid.* **112**, 563–576 (2018).
3. M. Genet *et al.*, Heterogeneous growth-induced prestrain in the heart. *J. Biomech.* **48**, 2080–2089 (2015).
4. D. W. Thompson, *On Growth and Form* (Cambridge University Press, 1917).
5. Y. Klein, E. Efrati, E. Sharon, Shaping of elastic sheets by prescription of non-Euclidean metrics. *Science* **315**, 1116–1120 (2007).
6. J. Huxley, F. Churchill, R. Strauss, *Problems of Relative Growth* (Johns Hopkins University Press, 1993).
7. J. Sachs, *Text-book of Botany: Morphological and Physiological* (Clarendon Press, 1875).
8. T. Tallinen *et al.*, On the growth and form of cortical convolutions. *Nat. Phys.* **12**, 588–593 (2016).
9. S. Budday, P. Steinmann, E. Kuhl, The role of mechanics during brain development. *J. Mech. Phys. Solid.* **72**, 75–92 (2014).
10. A. E. Shyer *et al.*, Villification: How the gut gets its villi. *Science* **342**, 212–218 (2013).
11. T. Savin *et al.*, On the growth and form of the gut. *Nature* **476**, 57–62 (2011).
12. H. Y. Kim *et al.*, Localized smooth muscle differentiation is essential for epithelial bifurcation during branching morphogenesis of the mammalian lung. *Dev. Cell* **34**, 719–726 (2015).
13. K. Goodwin *et al.*, Smooth muscle differentiation shapes domain branches during mouse lung development. *Development* **146**, dev181172 (2019).
14. J. Kim, J. A. Hanna, M. Byun, C. D. Santangelo, R. C. Hayward, Designing responsive buckled surfaces by halftone gel lithography. *Science* **335**, 1201–1205 (2012).
15. C. Modes, M. Warner, Shape-programmable materials. *Phys. Today* **69**, 32–38 (2016).
16. A. S. Gladman, E. A. Matsumoto, R. G. Nuzzo, L. Mahadevan, J. A. Lewis, Biomimetic 4D printing. *Nat. Mater.* **15**, 413–418 (2016).
17. S. Yang, K. Khare, P. C. Lin, Harnessing surface wrinkle patterns in soft matter. *Adv. Funct. Mater.* **20**, 2550–2564 (2010).
18. L. Hall-Stoodley, J. W. Costerton, P. Stoodley, Bacterial biofilms: From the natural environment to infectious diseases. *Nat. Rev. Microbiol.* **2**, 95–108 (2004).
19. G. O'Toole, H. B. Kaplan, R. Kolter, Biofilm formation as microbial development. *Annu. Rev. Microbiol.* **54**, 49–79 (2000).
20. J. K. Teschler *et al.*, Living in the matrix: Assembly and control of *Vibrio cholerae* biofilms. *Nat. Rev. Microbiol.* **13**, 255–268 (2015).
21. D. O. Serra, A. M. Richter, G. Klauck, F. Mika, R. Hengge, Microanatomy at cellular resolution and spatial order of physiological differentiation in a bacterial biofilm. *mBio* **4**, e00103-13 (2013).
22. D. O. Serra, A. M. Richter, R. Hengge, Cellulose as an architectural element in spatially structured *Escherichia coli* biofilms. *J. Bacteriol.* **195**, 5540–5554 (2013).
23. L. E. Dietrich *et al.*, Bacterial community morphogenesis is intimately linked to the intracellular redox state. *J. Bacteriol.* **195**, 1371–1380 (2013).
24. D. Romero, C. Aguilar, R. Losick, R. Kolter, Amyloid fibers provide structural integrity to *Bacillus subtilis* biofilms. *Proc. Natl. Acad. Sci. U.S.A.* **107**, 2230–2234 (2010).
25. J. Yan, C. D. Nadell, H. A. Stone, N. S. Wingreen, B. L. Bassler, Extracellular-matrix-mediated osmotic pressure drives *Vibrio cholerae* biofilm expansion and cheater exclusion. *Nat. Commun.* **8**, 327 (2017).
26. J. Yan *et al.*, Mechanical instability and interfacial energy drive biofilm morphogenesis. *eLife* **8**, e43920 (2019).
27. C. Zhang *et al.*, Experimental and theoretical studies on the morphogenesis of bacterial biofilms. *Soft Matter* **13**, 7389–7397 (2017).
28. M. J. Kirisits, L. Prost, M. Starkey, M. R. Parsek, Characterization of colony morphology variants isolated from *Pseudomonas aeruginosa* biofilms. *Appl. Environ. Microbiol.* **71**, 4809–4821 (2005).
29. M. T. Cabeen, S. A. Leiman, R. Losick, Colony-morphology screening uncovers a role for the *Pseudomonas aeruginosa* nitrogen-related phosphotransferase system in biofilm formation. *Mol. Microbiol.* **99**, 557–570 (2016).
30. S. Mukherjee *et al.*, The PqsE and RhlR proteins are an autoinducer synthase–receptor pair that control virulence and biofilm development in *Pseudomonas aeruginosa*. *Proc. Natl. Acad. Sci. U.S.A.* **115**, E9411–E9418 (2018).
31. F. H. Yildiz, G. K. Schoolnik, *Vibrio cholerae* O1 El Tor: Identification of a gene cluster required for the rugose colony type, exopolysaccharide production, chlorine resistance, and biofilm formation. *Proc. Natl. Acad. Sci. U.S.A.* **96**, 4028–4033 (1999).
32. F. Yildiz, J. Fong, I. Sadovskaya, T. Grard, E. Vinogradov, Structural characterization of the extracellular polysaccharide from Vibrio cholerae O1 El-Tor. *PLoS One* **9**, e86751 (2014).
33. J. C. Fong, F. H. Yildiz, The *rbmBCDEF* gene cluster modulates development of rugose colony morphology and biofilm formation in *Vibrio cholerae*. *J. Bacteriol.* **189**, 2319–2330 (2007).
34. V. Berk *et al.*, Molecular architecture and assembly principles of *Vibrio cholerae* biofilms. *Science* **337**, 236–239 (2012).
35. J. C. Fong *et al.*, Structural dynamics of RbmA governs plasticity of *Vibrio cholerae* biofilms. *eLife* **6**, e26163 (2017).
36. J. Yan *et al.*, Bacterial biofilm material properties enable removal and transfer by capillary peeling. *Adv. Mater.* **30**, 1804153 (2018).
37. C. Zhang, B. Li, X. Huang, Y. Ni, X. Q. Feng, Morphomechanics of bacterial biofilms undergoing anisotropic differential growth. *Appl. Phys. Lett.* **109**, 143701 (2016).
38. P. S. Stewart, M. J. Franklin, Physiological heterogeneity in biofilms. *Nat. Rev. Microbiol.* **6**, 199–210 (2008).
39. J. N. Anderl, J. Zahller, F. Roe, P. S. Stewart, Role of nutrient limitation and stationary-phase existence in *Klebsiella pneumoniae* biofilm resistance to ampicillin and ciprofloxacin. *Antimicrob. Agents Chemother.* **47**, 1251–1256 (2003).
40. A. Seminara *et al.*, Osmotic spreading of *Bacillus subtilis* biofilms driven by an extracellular matrix. *Proc. Natl. Acad. Sci. U.S.A.* **109**, 1116–1121 (2012).
41. S. Srinivasan, C. N. Kaplan, L. Mahadevan, A multiphase theory for spreading microbial swarms and films. *eLife* **8**, e42697 (2019).
42. J. Liu *et al.*, Metabolic co-dependence gives rise to collective oscillations within biofilms. *Nature* **523**, 550–554 (2015).
43. J. S. Madsen *et al.*, Facultative control of matrix production optimizes competitive fitness in *Pseudomonas aeruginosa* PA14 biofilm models. *Appl. Environ. Microbiol.* **81**, 8414–8426 (2015).
44. X. Chen, J. W. Hutchinson, Herringbone buckling patterns of compressed thin films on compliant substrates. *J. Appl. Mech.* **71**, 597–603 (2004).
45. Z. Huang, W. Hong, Z. Suo, Nonlinear analyses of wrinkles in a film bonded to a compliant substrate. *J. Mech. Phys. Solid.* **53**, 2101–2118 (2005).
46. M. B. Amar, M. Wu, Patterns in biofilms: From contour undulations to fold focussing. *Europhys. Lett.* **108**, 38003 (2014).
47. M. Asally *et al.*, Localized cell death focuses mechanical forces during 3D patterning in a biofilm. *Proc. Natl. Acad. Sci. U.S.A.* **109**, 18891–18896 (2012).
48. R. W. Ogden, *Nonlinear Elastic Deformations* (Courier Corporation, 1997).

49. E. K. Rodriguez, A. Hoger, A. D. McCulloch, Stress-dependent finite growth in soft elastic tissues. *J. Biomech.* **27**, 455–467 (1994).
50. A. Goriely, M. B. Amar, Differential growth and instability in elastic shells. *Phys. Rev. Lett.* **94**, 198103 (2005).
51. J. Dervaux, M. B. Amar, Morphogenesis of growing soft tissues. *Phys. Rev. Lett.* **101**, 068101 (2008).
52. J. W. Costerton, Z. Lewandowski, D. E. Caldwell, D. R. Korber, H. M. Lappin-Scott, Microbial biofilms. *Annu. Rev. Microbiol.* **49**, 711–745 (1995).
53. M. Wu, M. Ben Amar, Modelling fibers in growing disks of soft tissues. *Math. Mech. Solid* **20**, 663–679 (2015).
54. J. Monod, The growth of bacterial cultures. *Annu. Rev. Microbiol.* **3**, 371–394 (1949).
55. S. Budday, C. Raybaud, E. Kuhl, A mechanical model predicts morphological abnormalities in the developing human brain. *Sci. Rep.* **4**, 5644 (2014).
56. S. Walcott, S. X. Sun, A mechanical model of actin stress fiber formation and substrate elasticity sensing in adherent cells. *Proc. Natl. Acad. Sci. U.S.A.* **107**, 7757–7762 (2010).
57. P. Sens, Rigidity sensing by stochastic sliding friction. *Europhys. Lett.* **104**, 38003 (2013).
58. U. S. Schwarz, S. A. Safran, Physics of adherent cells. *Rev. Mod. Phys.* **85**, 1327–1381 (2013).
59. S. Chen, T. Bertrand, W. Jin, M. D. Shattuck, C. S. O'Hern, Stress anisotropy in shear-jammed packings of frictionless disks. *Phys. Rev. E* **98**, 042906 (2018).
60. S. Cai, D. Breid, A. J. Crosby, Z. Suo, J. W. Hutchinson, Periodic patterns and energy states of buckled films on compliant substrates. *J. Mech. Phys. Solid.* **59**, 1094–1114 (2011).
61. B. Audoly, A. Boudaoud, Buckling of a stiff film bound to a compliant substrate - Part I: Formulation, linear stability of cylindrical patterns, secondary bifurcations. *J. Mech. Phys. Solid.* **56**, 2401–2421 (2008).
62. M. B. Amar, F. Jia, Anisotropic growth shapes intestinal tissues during embryogenesis. *Proc. Natl. Acad. Sci. U.S.A.* **110**, 10525–10530 (2013).
63. F. Jia, M. B. Amar, Theoretical analysis of growth or swelling wrinkles on constrained soft slabs. *Soft Matter* **9**, 8216–8226 (2013).
64. P. Ciarletta, V. Balbi, E. Kuhl, Pattern selection in growing tubular tissues. *Phys. Rev. Lett.* **113**, 248101 (2014).
65. V. Balbi, E. Kuhl, P. Ciarletta, Morphoelastic control of gastro-intestinal organogenesis: Theoretical predictions and numerical insights. *J. Mech. Phys. Solid.* **78**, 493–510 (2015).
66. A Cont, T Rossy, Z Al-Mayyah, A Persat, Biofilms mechanically damage epithelia by buckling. *bioRxiv*, 2020.01.29.923060 (2020).
67. C. P. Kempes, C. Okegbe, Z. Mears-Clarke, M. J. Follows, L. E. Dietrich, Morphological optimization for access to dual oxidants in biofilms. *Proc. Natl. Acad. Sci. U.S.A.* **111**, 208–213 (2014).
68. M. B. Miller, B. L. Bassler, Quorum sensing in bacteria. *Annu. Rev. Microbiol.* **55**, 165–199 (2001).
69. B. K. Hammer, B. L. Bassler, Quorum sensing controls biofilm formation in *Vibrio cholerae*. *Mol. Microbiol.* **50**, 101–104 (2003).
70. Y. Shen *et al.*, Role of biofilm roughness and hydrodynamic conditions in *Legionella pneumophila* adhesion to and detachment from simulated drinking water biofilms. *Environ. Sci. Technol.* **49**, 4274–4282 (2015).
71. J. Dumais, S. L. Shaw, C. R. Steele, S. R. Long, P. M. Ray, An anisotropic-viscoplastic model of plant cell morphogenesis by tip growth. *Int. J. Dev. Biol.* **50**, 209–222 (2006).
72. B. He, K. Doubrovinski, O. Polyakov, E. Wieschaus, Apical constriction drives tissue-scale hydrodynamic flow to mediate cell elongation. *Nature* **508**, 392–396 (2014).
73. B. Guirao, Y. Bellaïche, Biomechanics of cell rearrangements in *Drosophila*. *Curr. Opin. Cell Biol.* **48**, 113–124 (2017).
74. O. Foubet, M. Trejo, R. Toro, Mechanical morphogenesis and the development of neocortical organisation. *Cortex* **118**, 315–326 (2018).
75. D. Matoz-Fernandez, F. A. Davidson, N. R. Stanley-Wall, R. Sknepnek, Wrinkle patterns in active viscoelastic thin sheets. *Phys. Rev. Res.* **2**, 013165 (2020).
76. J. N. Wilking *et al.*, Liquid transport facilitated by channels in *Bacillus subtilis* biofilms. *Proc. Natl. Acad. Sci. U.S.A.* **110**, 848–852 (2013).
77. J. Dervaux, J. C. Magniez, A. Libchaber, On growth and form of *Bacillus subtilis* biofilms. *Interface Focus* **4**, 20130051 (2014).
78. S. Haussler, C. Fuqua, Biofilms 2012: New discoveries and significant wrinkles in a dynamic field. *J. Bacteriol.* **195**, 2947–2958 (2013).
79. K. H. Thelin, R. K. Taylor, Toxin-coregulated pilus, but not mannose-sensitive hemagglutinin, is required for colonization by *Vibrio cholerae* O1 El Tor biotype and O139 strains. *Infect. Immun.* **64**, 2853–2856 (1996).
80. S. Beyhan, F. H. Yildiz, Smooth to rugose phase variation in *Vibrio cholerae* can be mediated by a single nucleotide change that targets c-di-GMP signalling pathway. *Mol. Microbiol.* **63**, 995–1007 (2007).
81. W. Thielicke, E. Stamhuis, PIVlab - towards user-friendly, affordable and accurate digital particle image velocimetry in MATLAB. *J. Open Res. Software* **2**, e30 (2014).
82. A. Zemel, F. Rehfeldt, A. Brown, D. Discher, S. Safran, Optimal matrix rigidity for stress-fibre polarization in stem cells. *Nat. Phys.* **6**, 468–473 (2010).
83. P. Marcq, N. Yoshinaga, J. Prost, Rigidity sensing explained by active matter theory. *Biophys. J.* **101**, L33–L35 (2011).
84. C. Geuzaine, J. F. Remacle, Gmsh: A 3-D finite element mesh generator with built-in pre-and post-processing facilities. *Int. J. Numer. Methods Eng.* **79**, 1309–1331 (2009).
85. H. Langtangen, K. Mardal, "Introduction to numerical methods for variational problems" in *Texts in Computational Science and Engineering*, T. J. Barth, M. Griebel, D. E. Keyes, R. M. Nieminen, D. Roose, T. Schlick, Eds. (Springer International Publishing, 2019), pp. 69–124.
86. M. Alnæs *et al.*, The FEniCS project version 1.5. *Arch. Numer. Software* **3**, 9–23 (2015).
87. J. Crank, P. Nicolson, "A practical method for numerical evaluation of solutions of partial differential equations of the heat-conduction type" in *Mathematical Proceedings of the Cambridge Philosophical Society* (Cambridge University Press, 1947), vol. 43, pp. 50–67.
88. E. Lejeune, A. Javili, C. Linder, Understanding geometric instabilities in thin films via a multi-layer model. *Soft Matter* **12**, 806–816 (2016).